Supplement of Atmos. Meas. Tech., 18, 4271–4292, 2025
https://doi.org/10.5194/amt-18-4271-2025-supplement

Atmospheric Measurement Techniques
Open Access
EGU

Supplement of

The role of fuel and environmental conditions on the amount and composition of primary, fresh, and aged aerosol emissions originating from diesel- and gasoline-operated auxiliary heaters of passenger cars

Henri Oikarinen et al.

Correspondence to: Henri Oikarinen (henri.oikarinen@uef.fi)

Table S1. Gaseous components measured by the FTIR from the raw exhaust gas.

Component	*Formula*	*Calibration range*	*Unit*	*VOC group*
Water vapor	H_2O	20	%	
Carbon dioxide	CO_2	25	%	
Carbon monoxide	CO	5000	ppm	
	CO	10000	ppm	
Nitrous oxide	N_2O	200	ppm	
Nitrogen monoxide	NO	1000	ppm	
Nitrogen dioxide	NO_2	200	ppm	
Sulfur dioxide	SO_2	1000	ppm	
Carbonyl sulfide	COS	100	ppm	
Ammonia	NH_3	500	ppm	
Hydrogen chloride	HCl	200	ppm	
Hydrogen cyanide	HCN	100	ppm	
Hydrogen fluoride	HF	100	ppm	
Oxygen	O_2	25	%	
Methane	CH_4	1000	ppm	Methane
Ethane	C_2H_6	100	ppm	Alkane
Propane	C_3H_8	100	ppm	Alkane
Butane	C_4H_{10}	100	ppm	Alkane
Pentane	C_5H_{12}	100	ppm	Alkane
Hexane	C_6H_{14}	100	ppm	Alkane
Heptane	C_7H_{16}	100	ppm	Alkane
Octane	C_8H_{18}	100	ppm	Alkane
Acetylene	C_2H_2	500	ppm	Unsaturated
Ethylene	C_2H_4	500	ppm	Unsaturated
Propene	C_3H_6	500	ppm	Unsaturated
1,3-Butadiene	C_4H_6	500	ppm	Unsaturated
Benzene	C_6H_6	500	ppm	Aromatic
Toluene	C_7H_8	100	ppm	Aromatic
m-Xylene	C_8H_{10}	100	ppm	Aromatic
o-Xylene	C_8H_{10}	200	ppm	Aromatic
p-Xylene	C_8H_{10}	100	ppm	Aromatic
1,2,3-Trimethylbenzene	C_9H_{12}	100	ppm	Aromatic
1,2,4-Trimethylbenzene	C_9H_{12}	100	ppm	Aromatic

1,35-Trimethylbenzene	C_9H_{12}	100	ppm	Aromatic
Formic acid	CH_2O	100	ppm	Oxygenated
Acetic acid	$C_2H_4O_2$	200	ppm	Oxygenated
Formaldehyde	CHOH	500	ppm	Oxygenated
Acetaldehyde	C_2H_4O	100	ppm	Oxygenated
Methanol	CH_4O	200	ppm	Oxygenated
Ethanol	C_2H_6O	200	ppm	Oxygenated
Propanol	C_3H_8O	100	ppm	Oxygenated
Methyl tert-butyl ether (MTBE)	$C_5H_{12}O$	100	ppm	Oxygenated
Phenol	C_6H_6O	200	ppm	Oxygenated aromatic
Furan	C_4H_4O	200	ppm	Oxygenated aromatic
Furfural	$C_5H_4O_2$	200	ppm	Oxygenated aromatic

S1. Experimental conditions in the environmental chamber during the laboratory experiments

The extent of OH exposure was estimated based on the decay of gasoline tracers (Barmet et al., 2012), which were monitored by the VOCUS-PTR. In the gasoline experiments, toluene in the exhaust itself was used as the tracer, and without H_2O_2 addition the [OH] was approximately similar as in ambient air (1.5×10^6 molec. cm^{-3}), so that atmospheric equivalent age of 4 hours was reached in the 4 hours (Fig. S1). For the diesel experiments with negligible toluene emissions and for the blank experiment, the exposure was estimated based on decay in an externally input tracer gas (butanol-d9), and the exposure was a factor of 10 higher with [OH] 1.5×10^7 molec. cm^{-3}.

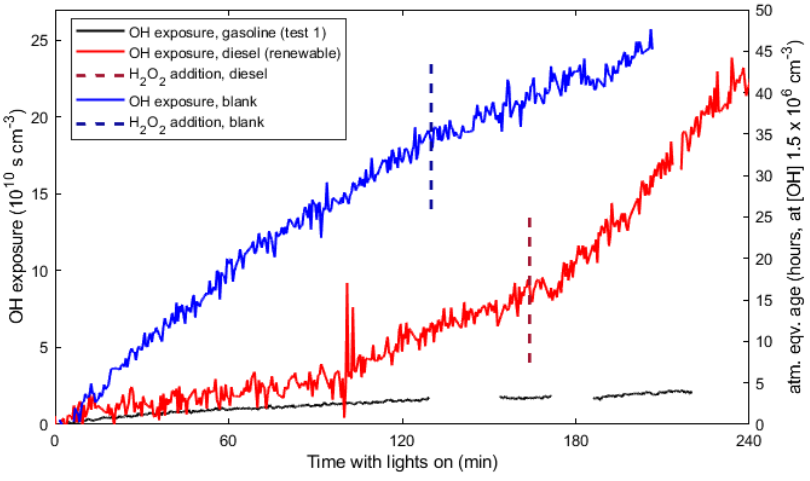

Figure S1. OH exposures during a gasoline experiment (test 1) and a diesel vehicle experiment (renewable fuel). Exposure in a blank experiment with H2O2 addition is also shown for comparison. Vertical lines denote the addition of H_2O_2 to the chamber.

The importance of gaseous wall losses was estimated for low-volatility organic compounds (LVOCs) similarly to (Palm et al. 2016) and (Hartikainen et al., 2023). The particulate condensation sink (CSPM; Fig. S2) in the chamber was calculated according to (Lehtinen et al. 2003, Boreal Environment Research 8(4):405-411) from the size distributions measured from the chamber. The CSPM increased rapidly after the initiation of photo-oxidation as the result of secondary aerosol formation and was in the range of 3×10^{-3} to 8×10^{-3} s^{-1} by the time of introduction to the TSAR.

The condensational sink of LVOCs to the chamber walls (CSwall) was 2.0×10^{-4} s^{-1} in the full chamber with 58.1 m^2 to 29.1 m^3 area-to-volume-ratio. During an experiment with sampling flow rates of 33.2 lpm or 43.9 lpm (with or without TSAR, respectively), CSwall increased to up to 2.8×10^{-4} s^{-1}. In other words, the LVOC loss to the chamber walls were in the same range as the CSPM for the cleanest diesel vehicle experiment. For the gasoline experiments, in contrast, the role of wall loss is minor, and the LVOCs condensed on the particle surfaces within minutes.

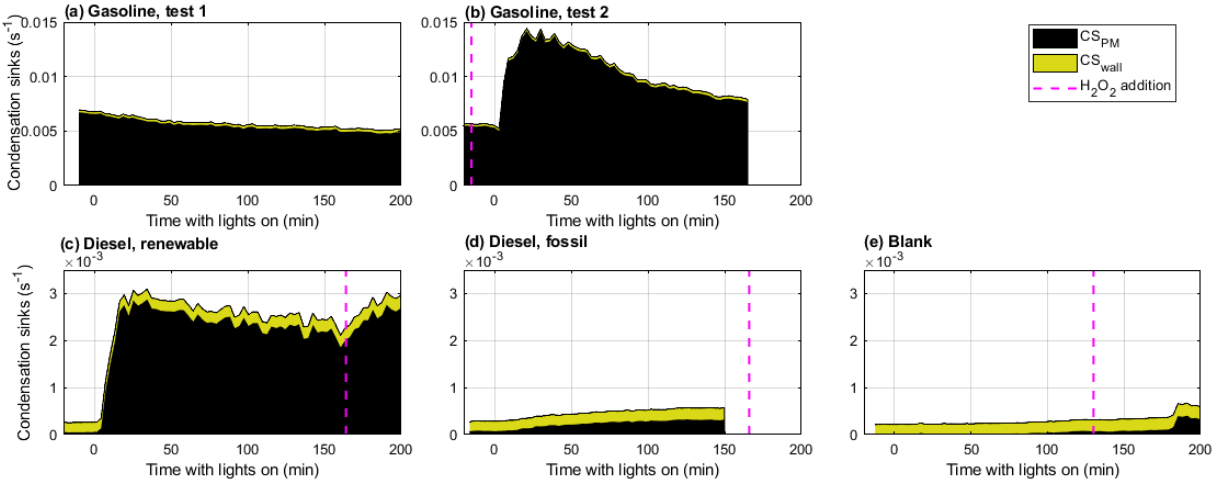

Figure S2. LVOC condensation sinks in the chamber.

S2. ELPI data inversion

Small particles deposit on ELPI upper collection plates (corresponding to large particle sizes) due to secondary collection mechanisms of smallest particles (e.g., diffusion) (Virtanen et al., 2001b). The extent of secondary collection was high especially when measuring downstream of TSAR because of the new particle formation in TSAR.

The effect of secondary collection is by default corrected in ELPI data processing: the amount of deposited small particles is determined based on the signals from the collection plates with cut-offs corresponding to the small particles. The secondary current resulting from smallest particles is then transferred from the upper collection plates to the lowest ones. (Moisio, 1999)

The secondary collection mechanisms depend on mobility diameter, not on the aerodynamic diameter that is measured by ELPI. Usually, the particles are assumed to have effective density of unity, so that the mobility size equals the aerodynamic size that is measured by ELPI. In this study, the assumption of unit density was not feasible. For example, Fig. S3 shows the untreated ELPI current distribution, and the current distribution after correcting for the secondary collection by assuming unit effective density. In the case shown in Fig. S3, the particles are formed from pure, particle-free dilution air oxidized in TSAR. Although the current observed at collection plates representing particles larger than 1 µm is decreased after the correction, they are still higher than 0 fA, indicating presence of particles larger than 1 µm.

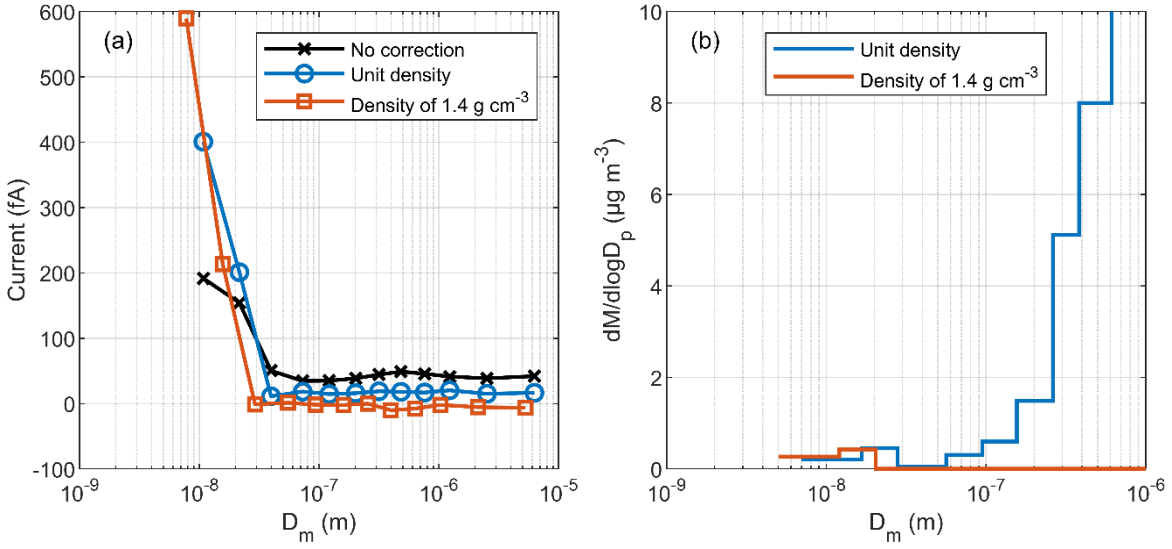

Figure S3. ELPI current distribution before and after correcting for secondary collection assuming different effective densities (a), and the resulting particle mass distribution with different effective densities (b).

However, it is highly unlikely that there would be particles larger than 1 μm formed in TSAR from purified air. Thus, using the assumption of unit effective density would lead to severe overestimation of the mass concentration.

When changing the effective density from 1.0 g cm^{-3} to 1.4 g cm^{-3} in the secondary collection correction, the currents from collection plates corresponding to large particles are very close to zero (Fig. S3a), and the corresponding particle mass size distribution (Fig. S3b) shows that all particle mass is located in particles smaller than 30 nm. When converting the current distributions in Fig. S3a to mass size distributions in Fig S3b, currents below 10 fA and currents that are less than 0.25% of total current were neglected.

According to the results above, it is necessary to find the correct effective density for each data point in order to avoid the error in the mass concentration caused by the secondary collection. The following algorithm was used to obtain the effective density of 1.4 g cm^{-3} in the Fig. S3 example:

- It was assumed that there are no particles larger than 1 μm in the sample; thus, the currents in 3 uppermost collection plates in ELPI (and 4 uppermost collection plates in ELPI+) should be close to zero after correcting for the secondary collection.
- The secondary collection correction was done for effective densities between 0.1 g cm^{-3} and 3.5 g cm^{-3} with 0.025 g cm^{-3} interval.
- The square sum of the currents at the three (or four in ELPI+) uppermost collection plates was calculated for each effective density at which the currents of the uppermost collection plates were below zero.
- The effective density at which the square sum was smallest was considered as the correct effective density.
- If no effective density was found where the currents of all three (or four) uppermost plates were below zero, only the two (or three) uppermost plates were considered. If the currents of these stages were not negative at any effective density, the requirement of negative current was discarded and only the minimum of the square sum was used to find the correct effective density.
- The effective density found with the algorithm was used in the final correction and when converting the corrected number size distribution into mass size distribution.
- In addition, currents below 10 fA and the currents that were less than 0.25% of total current were neglected. The currents here refer to currents after the secondary collection correction has been done.

The algorithm described above was conducted for each ELPI and ELPI+ data point at 1 Hz resolution.

In some cases, because of the high number of smallest particles and additional dilution, the signal from the coexisting larger particles was often too weak when measuring downstream of TSAR. For example, in Fig. S4, ELPI was measuring downstream of TSAR and ELPI+ upstream. In the upstream sample a mode of ~200 nm particles was measured, but this mode was not visible in the sample downstream of TSAR (measured with ELPI). Thus, the following additional algorithm was applied for all ELPI datapoints:

- If the ELPI+ signal in number size distribution is higher than the ELPI signal for collection plates with cut-off > 100 nm, the original ELPI signal is replaced with that of ELPI+.

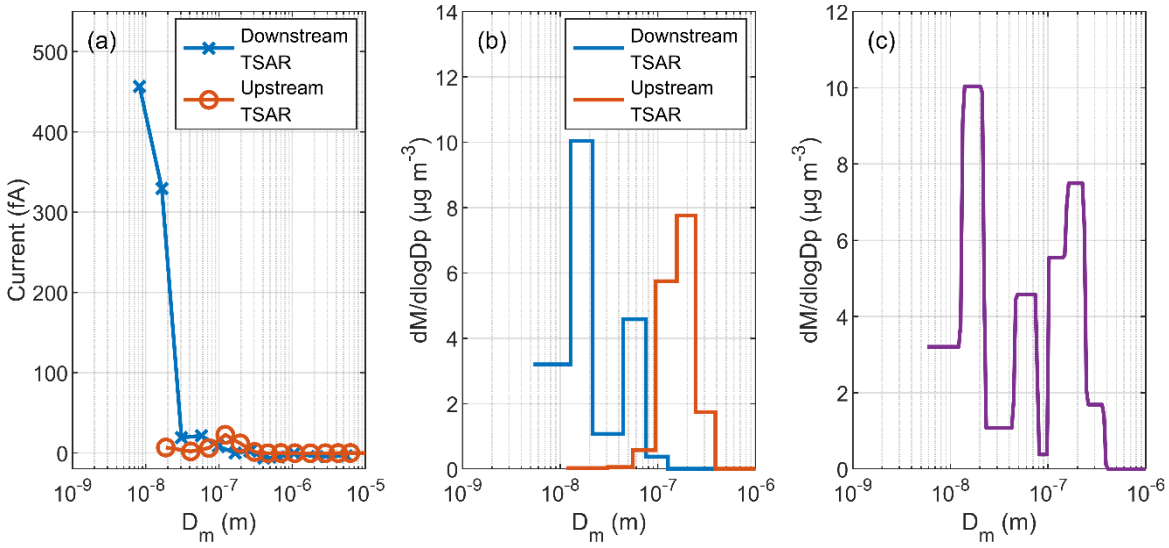

Figure S4. Combining ELPI distributions measured up- and downstream of TSAR. Corrected current distributions (a), mass distributions derived from the current distributions (b), and the combined mass distribution (c).

S3. Additional figures

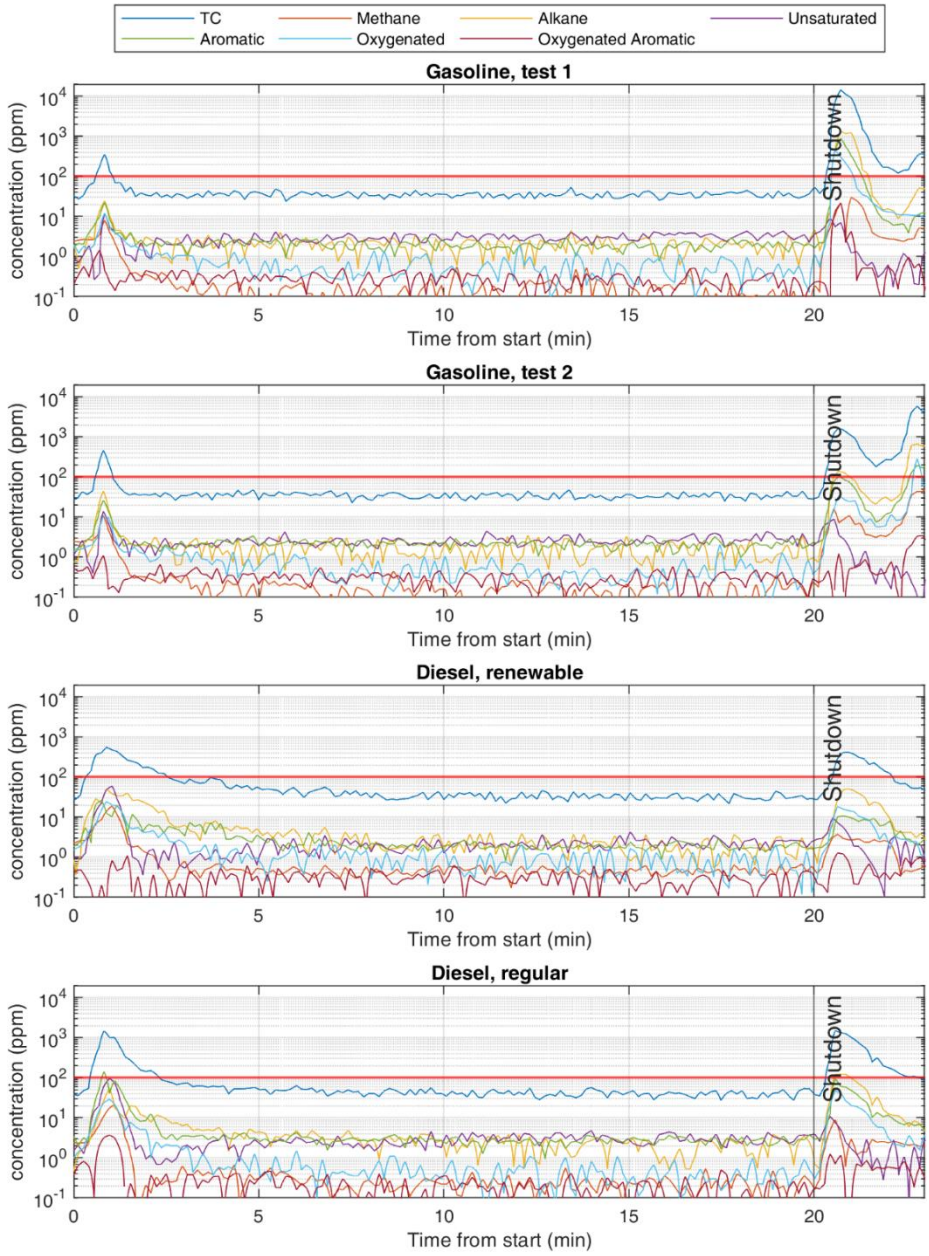

Figure S5. Hydrocarbon concentrations VOC groups from direct laboratory measurements measured with FTIR. Used VOC groups are the same as those presented in table S1, with further group of total carbon (TC) presenting sum of all VOC groups. The regulation limit for TC of 100 ppm is marked with horizontal red line.

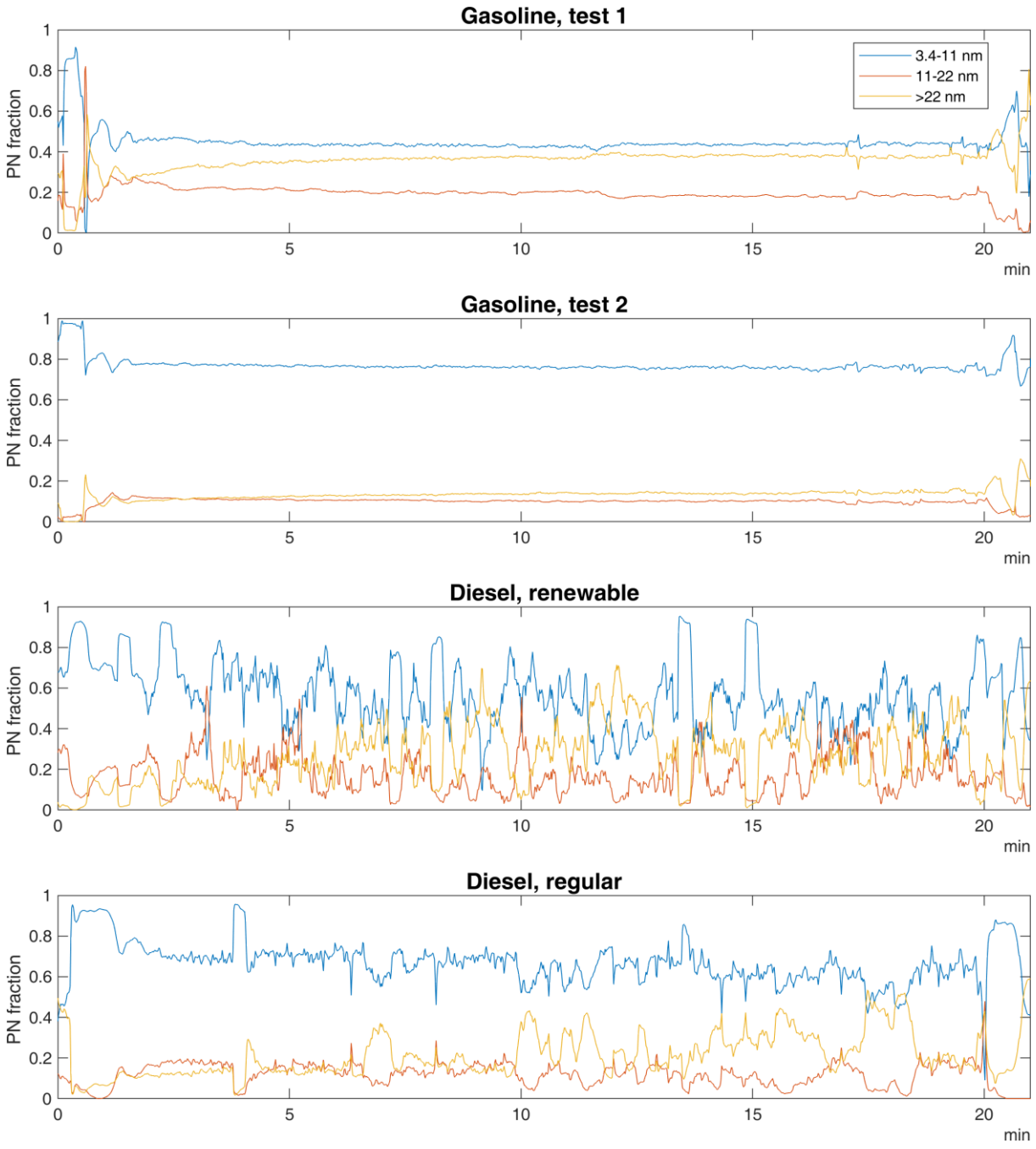

Figure S6. Direct CPC measurements from laboratory measurements for fractions of particles in size bins of 3.4-11 nm, 11-22 nm and >22 nm. Size bins are formed by subtracting from concentration of lower cut-off CPC the concentration of upper cut-off concentration. PN fraction is further calculated by comparing concentration of the size bin to total concentration measured with lowest cut-off (3.4 nm) CPC.

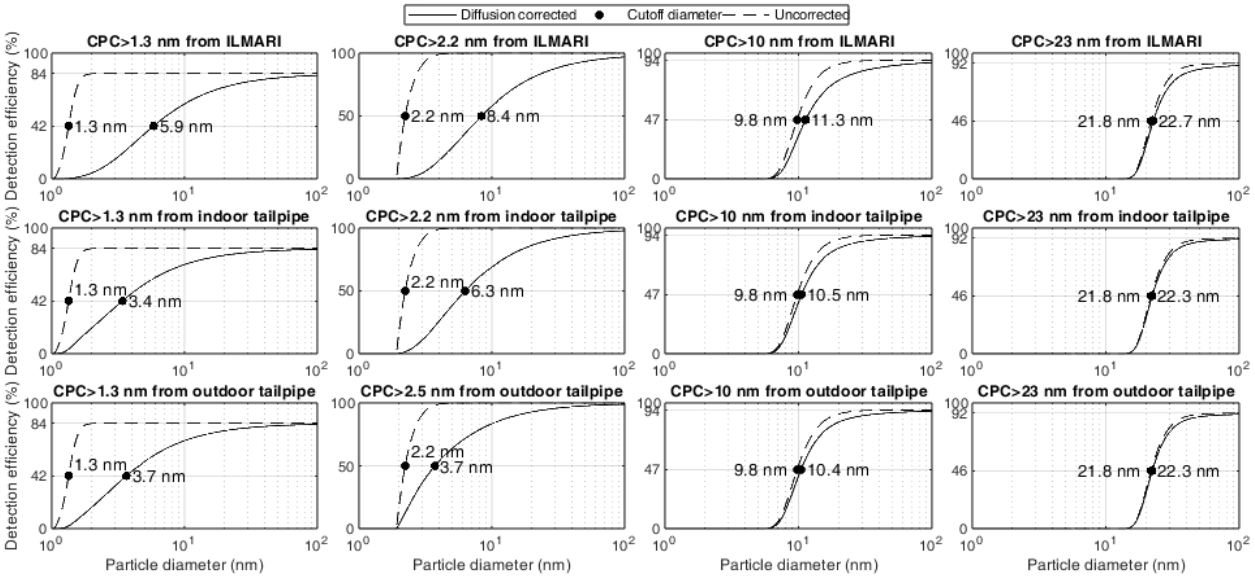

105 **Figure S7. Effective cut-off diameters of CPC-battery during laboratory measurements for both ILMARI chamber and tailpipe and for outdoor tailpipe measurements when diffusion losses in sampling lines are accounted for. Dashed line marks detection efficiency of each CPC and solid line marks line loss corrected detection efficiencies.**

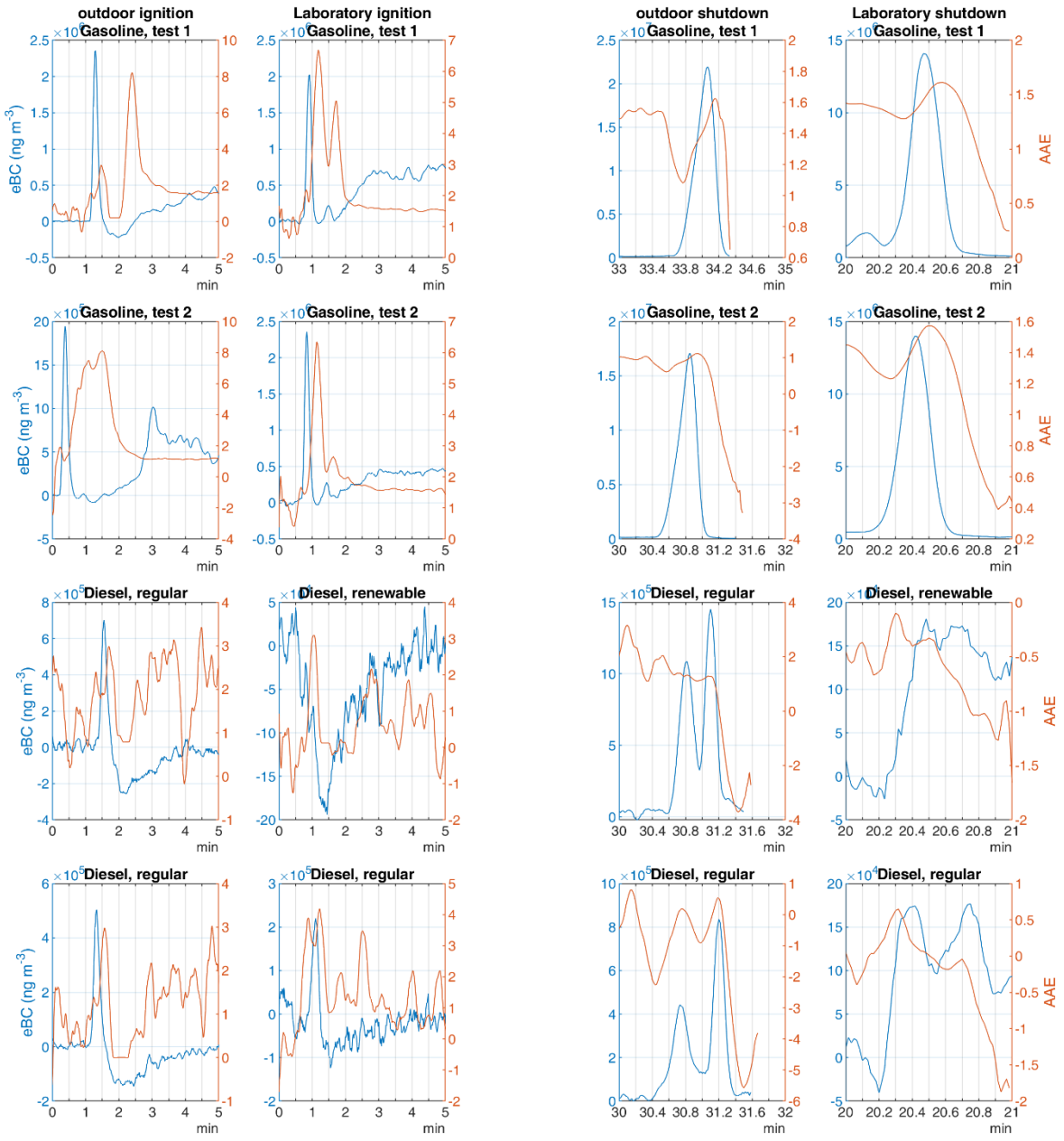

Figure S8. Comparision of ignition and shutdown spikes in eBC concentration and AAE measured for AHs for both outdoor and laboratory measurements.

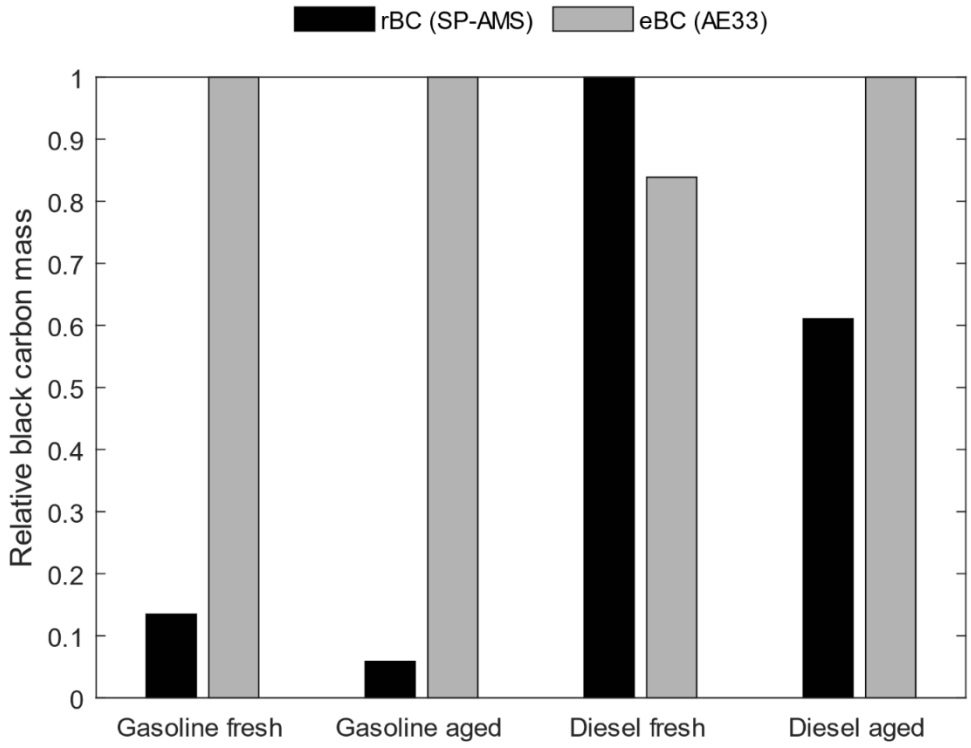

Figure S9. Comparison between rBC detected by the SP-AMS and BC detected by the AE33. The values are normalized to the larger of the two for each case.

115

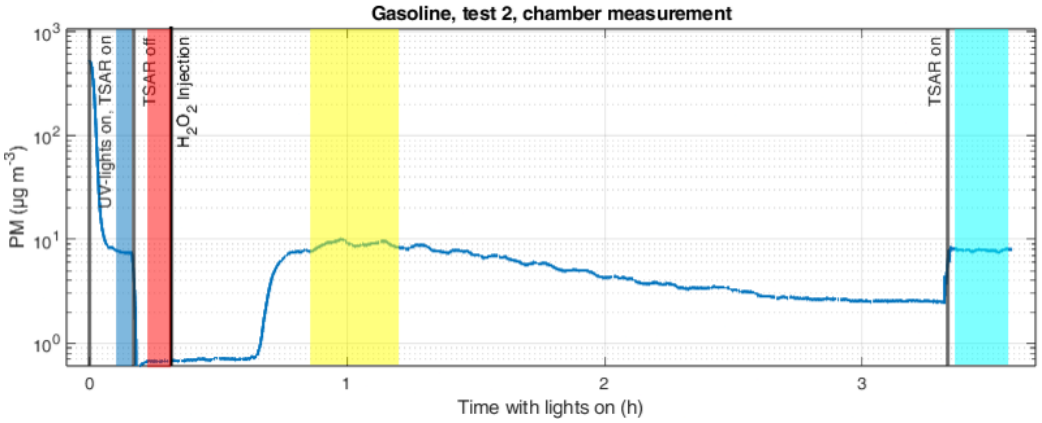

Figure S10. Example of PM changes during chamber measurement. Colored areas of the plot correspond to PM mass concentrations used to calculate PM EFs for Fig. 9. Red area corresponds to Fresh EF, blue area on the left side matches TSAR aged EF, yellow area to Chamber aged EF with H2O2 injection, and turquoise area to both chamber and TSAR aged EF. It should be noted that only PM mass measurements included the possibility of TSAR aging, so for other substances only fresh and chamber aged EFs are available.

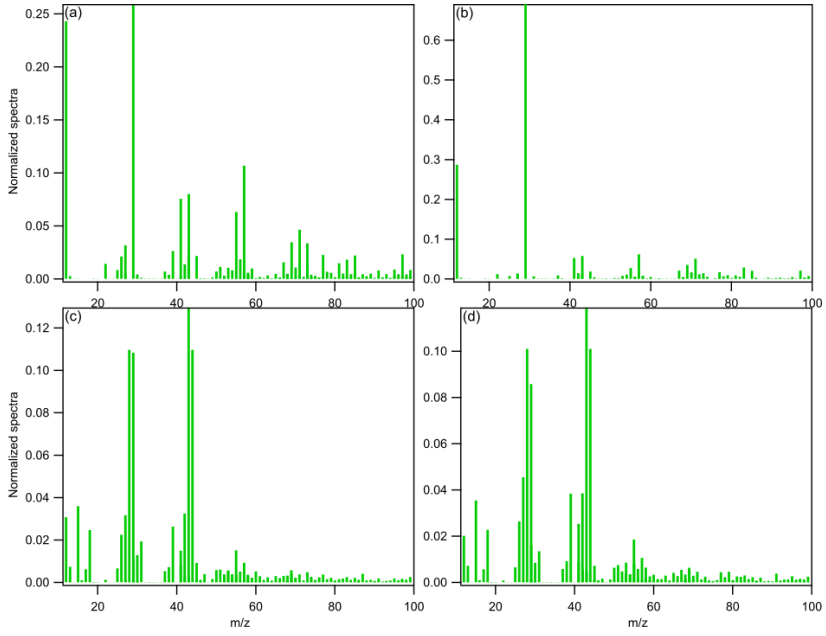

Figure S11. Normalized organic mass spectra of (a) gasoline fresh emissions, (b) diesel fresh emissions, (c) gasoline aged emissions and (d) diesel aged emissions.